Drying of silty soil treated with superabsorbent hydrogels
Retention behaviour and cracking

Liaudat, Joaquín; Muraro, Stefano

DOI
10.1016/j.enggeo.2024.107433
Publication date
2024
Document Version
Final published version
Published in
Engineering Geology

Engineering Geology 331 (2024) 107433

Contents lists available at ScienceDirect

Engineering Geology

journal homepage: www.elsevier.com/locate/enggeo

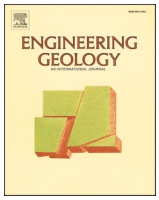

Drying of silty soil treated with superabsorbent hydrogels: Retention behaviour and cracking

Joaquín Liaudat *, Stefano Muraro

Department of Geoscience and Engineering, Delft University of Technology, 2628, CN, Delft, The Netherlands

ARTICLE INFO

Keywords:
Soil
Desiccation cracking
Superabsorbent hydrogels

ABSTRACT

Desiccation cracks in soils pose risks to the serviceability and safety of geotechnical infrastructure worldwide. This paper aims to investigate the potential of superabsorbent hydrogels (SAH) as innovative soil amendment to mitigate soil drying effects and cracking. Laboratory tests were conducted on an initially saturated silty soil treated with different types and dosages of SAH. Desiccation cracking tests, shrinkage tests, and water retention tests were performed to analyse the cracking process, evaporation rate, and retention properties. The tests were integrated with micro-CT scan analyses to observe changes in soil fabric due to the SAH addition. The results indicate that SAH particles serve as internal water reservoirs, extending the normal shrinkage stage and maintaining higher suctions without significant desaturation, in comparison to untreated soil. The addition of SAH reduces the evaporation rate, particularly at a dosage of 0.1%. The progression of cracking occurs at suctions below the air entry value, and the inclusion of SAH reduces the rate of crack development. These findings highlight the need for additional research on SAH as a promising soil treatment for geotechnical applications.

1. Introduction

The formation of desiccation cracks in soils is a common natural phenomenon widely observed in nature. In recent years, concerns have arisen regarding the impact of desiccation cracks on existing geotechnical infrastructure, such as transportation systems, flood defences, and landfills, due to changes in climate patterns. Desiccation cracks can pose risks to the serviceability and safety of geo-infrastructures by reducing their water-holding capacity, increasing hydraulic conductivity, raising soil compressibility, and decreasing soil shear strength (Khan et al., 2017; Li et al., 2017; Morris et al., 1992; Song and Cui, 2020; Zhang et al., 2021).

These cracks typically appear after prolonged periods of drought, leading to long-term soil drying and a subsequent decrease in water content. During this drying process, the soil tends to shrink due to the development of suction in the matrix. If this shrinkage is restrained, tensile stresses develop within the soil mass, eventually leading to cracking (Cheng et al., 2020; Corte and Higashi, 1964; Peron et al., 2009). Shrinkage restraint can occur due to differential shrinkage in the soil mass, stiffness heterogeneity caused by inclusions such as voids, boulders, sand grains, and roots, or restrictions arising from soil-structure interactions (Peron et al., 2009).

In addition to the large body of research undertaken to investigate the initiation and propagation of desiccation cracks in soils, research has been carried out in recent decades on admixtures to modify the desiccation cracking process. These admixtures include chemical additives (e.g. lime, cement and fly ash), synthetic and natural fibres, bio-minerals (e.g., microbially and enzyme induced calcite precipitation) and more recently nanoparticles. A comprehensive review of the different methods is provided by Tang et al. (2021).

Along this line, this paper explores the potential of a different kind of admixture known as superabsorbent hydrogels (SAH) to mitigate soil desiccation cracking. Superabsorbent hydrogels, also termed as superabsorbent polymers or water-absorbing polymers, consist of cross-linked three-dimensional polymer networks, with carboxyl groups, amino groups, hydroxyl groups or other hydrophilic groups attached to a polymeric backbone (Bao et al., 2011; Feng et al., 2014). Because of this structure, SAH can absorb and retain substantial amounts of water and solute molecules in a swollen state (Feng et al., 2014; Ismail et al., 2013; Spagnol et al., 2012). Due to this exceptional hydrophilicity, SAH are used in many fields such as drug delivery, tissue engineering, biosensors, food storage, wastewater treatment and hygiene products (Bao et al., 2011; Ismail et al., 2013).

In recent years, SAH have been increasingly used as a soil amend-

* Corresponding author.
E-mail addresses: J.Liaudat@tudelft.nl (J. Liaudat), S.Muraro@tudelft.nl (S. Muraro).

https://doi.org/10.1016/j.enggeo.2024.107433
Received 25 July 2023; Received in revised form 5 December 2023; Accepted 2 February 2024
Available online 6 February 2024

ment for drought management in agriculture, horticulture, and forestry (Saha et al., 2020b). Several studies have reported that small additions (<1 wt%, weight percent) of SAH can significantly increase the water retention capacity of the treated soil, thereby reducing the water loss by evaporation or deep percolation (Andry et al., 2009; Bakass et al., 2002; Banedjschafie and Durner, 2015; Dorraji et al., 2010; Koupai et al., 2008; Liao et al., 2016; Montesano et al., 2015; Narjary et al., 2012; Saha et al., 2020a; Yu et al., 2017). However, the specific effects on the water retention characteristics in terms of saturated water content, air entry value, and residual water content vary considerably depending on the soil type (Koupai et al., 2008; Saha et al., 2020a).

Because of these effects on the water retention properties, the addition of SAH is expected to influence the soil desiccation cracking process. However, research in this aspect has been limited so far. In a series of laboratory desiccation cracking tests on a clayey soil, Qi et al. (2020) assessed the effect of polyurethane (PU) and polyacrylamide (PAM) admixtures. Different concentrations between 0.25 and 1 wt% for PU and between 0.025 and 0.1 wt% for PAM were tested. The results revealed that the addition of PU slightly increases the final Crack Intensity Factor (CIF), which represents the ratio between the crack area and the initial area of the soil surface. In contrast, the addition of PAM led to a small, non-monotonic decrease in the final CIF. However, the authors did not report data on the kinetics of the cracking process.

In a similar laboratory study, Taheri and El-zein (2023) investigated the effect of adding sodium carboxymethyl cellulose (Na-CMC) in concentrations of 2 and 4 wt% on the desiccation cracking of bentonite clay. They found that the addition of Na-CMC delays the cracking initiation and significantly reduces the CIF. However, these parameters do not vary monotonically with the dosage, i.e., the cracking initiates later and the final CIF is smaller for specimens with 2 wt% of Na-CMC compared to those with 4 wt%.

This paper presents an experimental investigation into the desiccation cracking behaviour of a silty soil treated with three types of commercially available SAH with different characteristics. The study combines desiccation cracking tests with shrinkage and retention data. This combination offers both qualitative and quantitative insights into the effects of SAH on soil water evaporation, shrinkage, and cracks initiation and propagation. The laboratory tests are complemented with micro-CT scan analyses to examine potential soil fabric changes due to the SAH addition.

2. Materials

The soil used in this study was retrieved from a dike in Maasdijk near Oijen (The Netherlands). The soil properties are summarised in Table 1. The soil was first dried, ground, and passed through a sieve 425 μm. The specific gravity of the soil, G_s, was measured with a helium pycnometer (ASTM, 2014) and the particle size distribution was obtained from wet-sieving and hydrometer analysis (BS, 1996).

Three different types of commercially available SAH have been evaluated. For the sake of brevity, they are referred to as SAH types F, S and P. Hydrogel type F is a granular anionic polyacrylamide polymer with grain size 0.0–0.3 mm. It is a cross-linked copolymers of acrylamide and potassium acrylate, commercialised by SNF Floerger (France) under the brand name 'Floset 27 CS'. Hydrogel type S is a fine powder, high-weighted, linear polyacrylic acid with average molar mass $M_v = 4,000,000$ g/mol and ~0.1% cross-linkage, from Sigma-Aldrich (Germany). Hydrogel type P is a granular sodium polyacrylate polymer with grain size 0.1–1.0 mm, provided by HRT POLSKA (Poland). Fig. 1 shows optical microscope images of the particles of the three types of hydrogels.

Table 1
Soil properties.

Soil property	Value
Specific gravity	2.64
Liquid limit	33%
Plastic limit	20%
Plastic Index	13%
Sand (60μm – 425μm)	5.7%
Silt (2μm – 60μm)	63.7%
Clay (< 2μm)	30.6%

All samples in this study were prepared using de-ionised water. Typically, the water absorption capacity of SAH in de-ionised water can reach several hundred times the dry weight of the hydrogel (Rizwan et al., 2021). For this paper, the water absorption capacities of SAH types F and P were measured following the procedure proposed by Cheng et al. (2017), resulting in water-to-SAH weight ratios of 458 and 386, respectively. Attempts to measure the water absorption capacity of type S with this procedure failed due to its extremely fine particle size (Fig. 1). It is important to note, however, that the absorption capacity may be significantly reduced when mixed with soil due to the mechanical constraint of the soil skeleton (Louf et al., 2021) and the presence of salts dissolved in the pore water (Rizwan et al., 2021).

3. Desiccation cracking

3.1. Methods

Desiccation tests were conducted on slurry samples treated with the three types of SAH and with three different dosages to assess the impact of SAH on the desiccation cracking response. All specimens were prepared with the same initial average water content, $w = 100\%$ (1 g of water per g of dry soil), but varying types and dosages SAH as specified in Table 2. For comparison, a reference specimen without SAH treatment was also tested. The dosage of SAH is expressed as dry mass of SAH per unit mass of dry soil. The SAH and soil were first mixed in dry condition before adding the water. The slurries were then manually mixed in individual containers with air-tight lids. After mixing, the slurries were left in the container overnight with the lids on to ensure hydration of the SAH and soil while preventing water evaporation. After this resting period, the slurries were poured into square PMMA (polymethyl methacrylate) trays with inner dimensions 87 × 87 × 43 mm and gently vibrated to achieve a flat top surface. One specimen was prepared per each SAH type and dosage combination given in Table 2. All specimens had similar dry soil content, approximately 111 g.

Shortly after filling the moulds, water segregation was observed in all the specimens. It can be appreciated in Fig. 2 that the amount of segregated water decreases and the thickness of the slurry layer increases with increasing SAH content. The same pattern was consistently observed for all three types of SAH. The reference specimen exhibited a similar degree of water segregation as the specimens with 0.1% SAH. Following the filling of the moulds, the specimens were placed on top of a table in a climate-controlled room. Throughout the preparation of the specimens and the subsequent desiccation cracking tests, the average temperature and relative humidity were maintained at 17.7 ± 1.0 °C and 71.5 ± 5.0%, respectively.

The specimens were weighed with a resolution of 0.01 g and photographed at intervals to track the desiccation process. The pictures were captured using a Canon EOS 750D camera with an EFS 18–135 mm lens. The camera was mounted on a copy stand equipped with daylight fluorescent lamps, and connected to a computer via a USB cable (Fig. 3). Canon EOS Utility software was used to focus, shoot, and store the pictures in the computer. L-profiles guides were attached to the copy stand to ensure consistent positioning of the specimens.

The captured pictures were treated to obtain the evolution of the Crack Intensity Factor (CIF) during the desiccation process. The initial images were cropped to a Region of Interest (ROI) of 80 × 80 mm in the centre of the specimen (Fig. 4a and b). The cropped images were segmented into two regions, namely soil clods and cracks, using an iterative region-growing algorithm proposed by Chan and Vese (2001) (Fig. 4c), which is available in the MATLAB Image Processing Toolbox

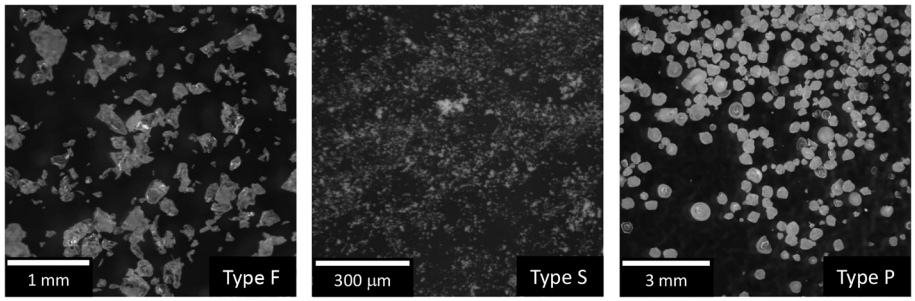

Fig. 1. Optical microscope images of the three types of hydrogel considered.

Table 2
Specimens considered in the desiccation cracking tests.

ID	Hydrogel	Dosage
Ref.	none	n/a
F-0.1	Type F	0.1%
F-0.5	Type F	0.5%
F-1.0	Type F	1.0%
S-0.1	Type S	0.1%
S-0.5	Type S	0.5%
S-1.0	Type S	1.0%
P-0.1	Type P	0.1%
P-0.5	Type P	0.5%
P-1.0	Type P	1.0%

(The MathWorks, 2020). The CIF of the ROI was calculated as the ratio between the crack area (yellow zone in Fig. 4c) and the total area of the ROI. Additionally, the Total Crack Length (TCL) was manually determined in selected pictures (Fig. 4d).

The test concluded when the specimens reached constant weight condition. At this time, X-ray computed micro-tomography (micro-CT) was performed on clod samples (approximately 10 × 20 × 20 mm) extracted from both the reference specimen and the specimens treated with type F SAH. This analysis aimed to evaluate the effect of SAH addition on the soil fabric. The micro-CT were carried out using the Phoenix Nanotom 180 NF system (Waygate Technologies), with a resolution of 15 μm. The samples were scanned with X-rays set to 110 kV source voltage and a current of 0.16 mA at the target. The source-to-target and source-to-detector distances were set to 90 and 300 mm, respectively. The micro-CT volumes were reconstructed and segmented using Avizo software (Thermo Fisher Scientific, 2020).

3.2. Results

Fig. 5 shows the time evolution of the average water content for the specimens with SAH, grouped by SAH type, and the reference untreated specimen. The qualifier 'average' is introduced to highlight that the water content is obtained based on the total amount of water and dry soil in the trays. The final average water content was cross-checked with oven dried weight at 105 °C, showing differences below 1%. In all cases, the water content evolution shows the typical pattern, with an initial stage with constant evaporation rate while the soil remains saturated, followed by a falling rate stage as air enters the soil matrix Tang et al. (2021). The evaporation rate at the initial state, $\dot{W}$, obtained by linear fitting is reported in Table 3. The results clearly demonstrate that the addition of SAH reduces the desiccation rate of the specimens in comparison with the reference specimen. The most significant reductions are observed in the specimens treated with type F SAH, followed by those treated with type S and type P. Notably, the reduction of the desiccation rate is not proportional to the amount of SAH added. The highest reduction of the desiccation rate is observed at a dosage of 0.1%, followed by 0.5% and 1.0%. This trend is consistent across all three types of SAH tested.

Figs. 6 and 7 show the evolution of the CIF with time and with the specimen average water content, respectively, grouped by SAH type. The experimental data exhibit three distinct stages in the cracking processes. These data are fitted using tetra-linear functions, as displayed in Fig. 8. The parameters t_0 and t_2 indicate the initiation and termination times of the cracking process, respectively. Inspection of the specimen pictures reveals that t_1 corresponds to the time at which there is no further propagation of existing cracks nor appearance of new cracks. The increase in the CIF after t_1 is only due to further widening of existing cracks. The parameters w_0, w_1 and w_2 represent the same turning points in the cracking process as t_0, t_1 and t_2, but in terms of specimen average water content instead of time. For all cases, the goodness-of-fit parameter R^2 exceeds 0.998. The fitted values are reported in Table 3.

Fig. 3. Camera and lighting setup.

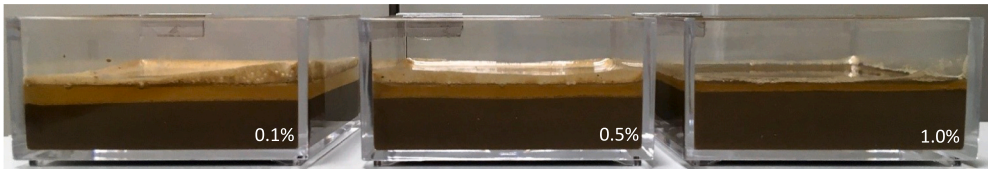

Fig. 2. Lateral view of specimens with different SAH dosage at the beginning of the desiccation cracking test.

(a) Initial image (b) Cropped 80×80 mm ROI (c) Segmented cracks (d) Total Crack Length

Fig. 4. Image post-processing.

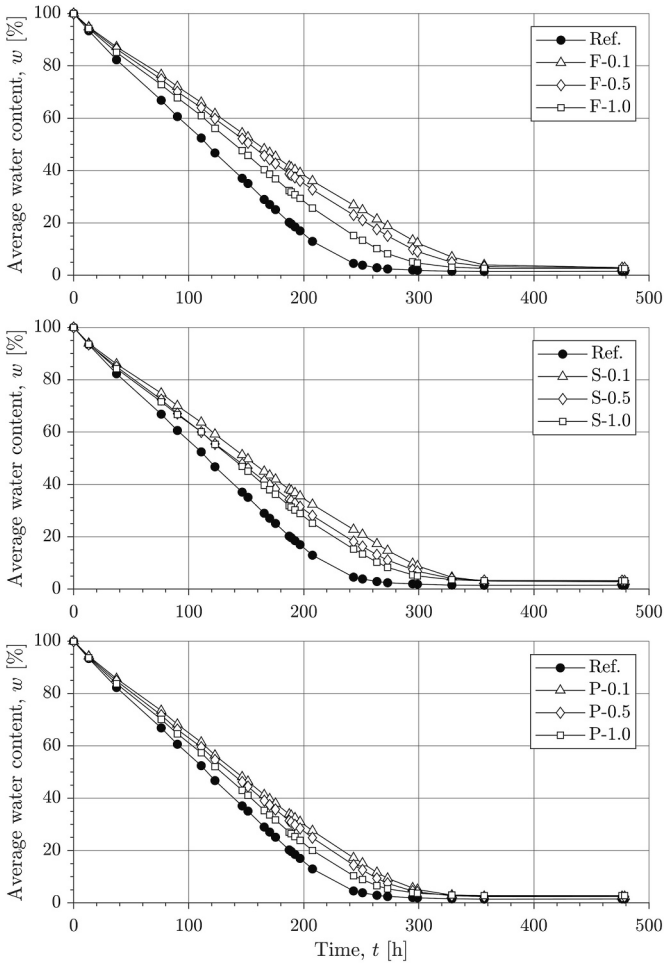

Fig. 5. Time evolution of the specimen average water content.

The fact that there is no further crack propagation after t_1 is additionally supported by Fig. 9, which shows the evolution of Total Crack Length (TCL) for both the reference specimen and the specimen with 1% of SAH type F. In both cases the TCL stabilises at time t_1.

The results of the desiccation tests, displayed in Figs. 6 and 7, are further elaborated by analysing the parameters of the tetra-linear fitting functions for varying dosages of SAH. Fig. 10a and c show the effect of SAH addition on the initiation of the cracking process (i.e., parameters t_0 and w_0). The dashed lines indicate the results for the reference specimen. The results are consistent across the three types of SAH. Compared to the reference specimen, the cracking initiation time is significantly delayed for low SAH content (0.1%), slightly delayed for 0.5% SAH content, and conversely, accelerated for high content (1.0%). In contrast, the average water content at the cracking initiation increases monotonically with the SAH content (Fig. 10c).

Fig. 10b and d show the duration ($t_2 - t_0$) and the range of water content ($w_0 - w_2$) over which the cracking process develops, as functions of the SAH type and dosage. In general, the trend is similar for all three SAH types, as cracks form over a longer period and broader ranges of water content with increasing SAH content.

Fig. 10e displays the effect of SAH addition on the final CIF (parameter c_2). The specimens treated with SAH type F consistently exhibit a reduction in the final CIF, ranging between 8 and 18% across all dosages. In contrast, the specimens treated with SAH type S and P displayed a decrease of the final CIF for low dosage and an increase at high dosage.

Fig. 10f shows the effect of SAH addition on the final TCL. For all SAH types, the results demonstrate a monotonic decrease of the final TCL with the dosage, except for specimen S-0.1 which exhibits a lower TCL than specimen S-0.5.

Fig. 11 shows horizontal slice images of clod samples (10 × 13 mm) obtained using micro-CT at the conclusion of the desiccation cracking tests. The samples include the reference specimen and three specimens treated with SAH type F. In these images, the grey level represents the relative density of the material components, ranging from black for air-filled voids to nearly white for sand grains. The effect of adding SAH (type F) on the dry soil fabric is evident. As the dosage of SAH is increased, the volume of air-filled voids (black zones in the images) also increases. Moreover, two different voids morphologies can be observed:

Table 3
Initial evaporation rate ($\dot{W}$) and fitted parameters of the tetra-linear functions defined in Fig. 8.

ID	$\dot{W}$ [g/h]	t_0 [h]	t_1 [h]	t_2 [h]	w_0 [%]	w_1 [%]	w_2 [%]	c_1 [−]	c_2 [−]
Ref.	0.486	153.4	181.0	246.0	33.8	23.2	3.8	0.109	0.141
F-0.1	0.351	207.5	255.9	337.3	36.1	23.9	5.4	0.089	0.122
F-0.5	0.368	160.2	211.2	304.1	47.3	31.9	7.8	0.095	0.131
F-1.0	0.406	113.3	173.0	277.3	59.8	38.1	6.8	0.089	0.116
S-0.1	0.372	192.8	245.5	312.7	36.6	22.5	5.6	0.106	0.134
S-0.5	0.423	153.2	208.4	305.0	44.7	29.8	6.0	0.117	0.147
S-1.0	0.394	78.7	155.1	280.2	70.8	46.2	5.0	0.118	0.166
P-0.1	0.387	189.8	217.2	299.7	33.2	25.0	4.6	0.089	0.120
P-0.5	0.420	168.2	201.4	275.2	38.1	27.2	6.3	0.092	0.134
P-1.0	0.436	110.9	189.3	265.6	57.3	26.7	5.5	0.124	0.159

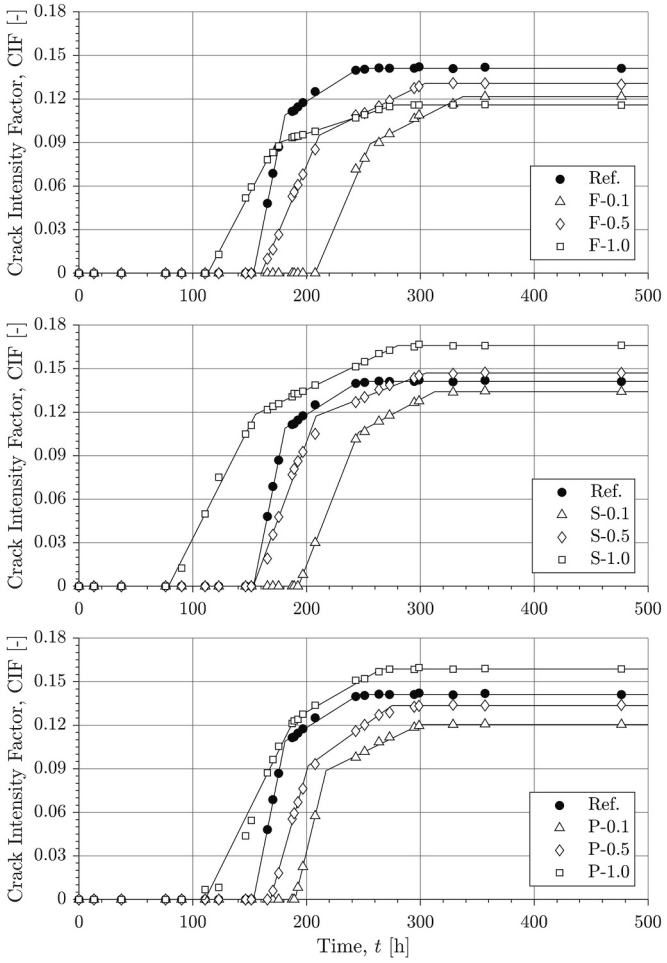

Fig. 6. Time evolution of the Crack Intensity Factor. Continuous lines are tetra-linear fitting functions.

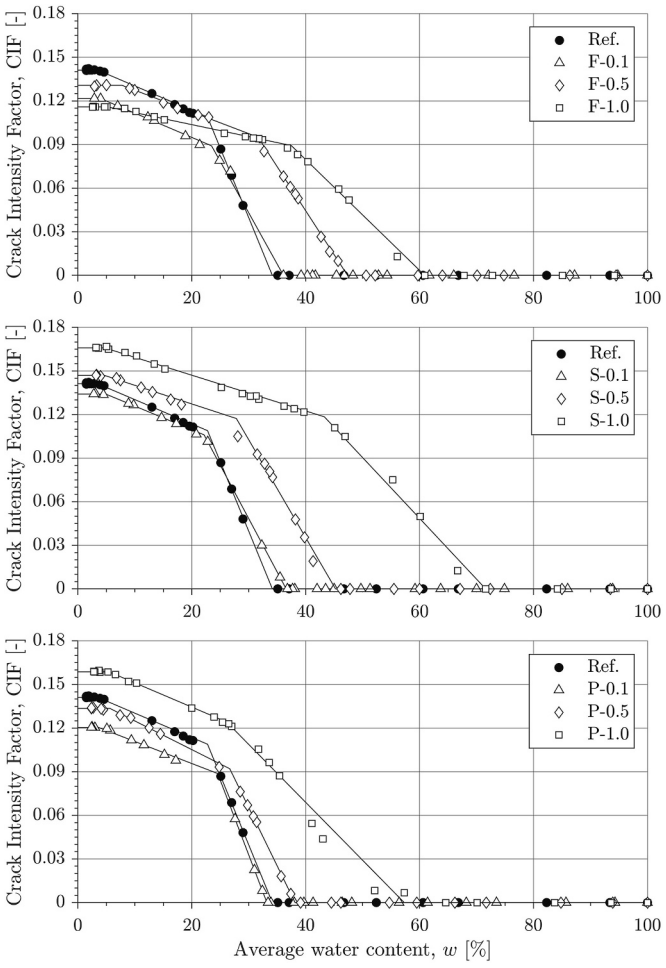

Fig. 7. Evolution of the Crack Intensity Factor with the specimen average water content. Continuous lines are tetra-linear fitting functions.

spherical/ellipsoidal voids and angular-shaped voids. The angular voids are exclusive to the samples treated with SAH. In contrast, spherical voids, likely resulting from air bubbles trapped in the slurry during the mould-filling process, are present in all samples, although, trapped air bubbles are bigger and more frequent in the samples with SAH. The increasing matrix inhomogeneity and possible flaws due to hydrated SAH and trapped air bubbles could have an influence on the increase in the average water content at cracking initiation (w_0) with the SAH dosage (Fig. 10c).

4. Fabric evidence

4.1. Methods

To evaluate the effect of SAH on the soil fabric, two slurry specimens, one with and the other without SAH, were periodically scanned using micro-CT in a cycle of drying and re-wetting. The initial average water content was $w = 60\%$ for both specimens. The specimen with SAH was prepared with type F SAH, because it showed the most promising results in the desiccation cracking tests (Sec. 3). When selecting the dosage, an intermediate value of 0.35% was adopted. This choice fell within the range where the results in Sec. 3 were most promising (0.1% to 0.5%) and provided a substantial number of SAH particles for micro-CT imaging.

Similar to the previously discussed desiccation cracking tests, the slurries were manually mixed in individual containers and left overnight with airtight lids to guarantee hydration of the SAH and soil particles.

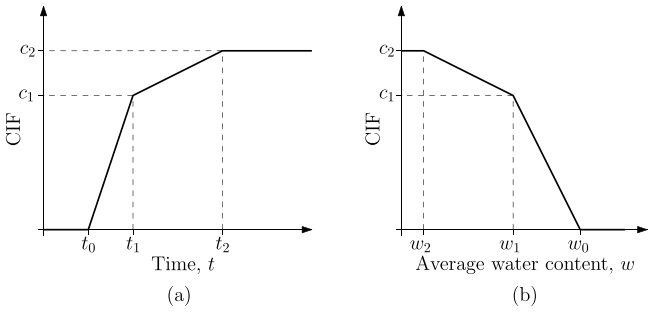

Fig. 8. Tetra-linear fitting functions.

After this period, each slurry was poured into cylindrical PPCO (polypropylene copolymer) jars with air-tight closure and inner dimensions Ø33 × 66 mm. The jars were gently vibrated to achieve a flat surface on the slurry. Due to the lower initial water content, no water segregation was observed. The slurry thickness in both jars was around 20 mm, and the dry soil weight was approximately 20 g. The change of the specimen geometry with respect to Sec. 3 was driven by both the geometrical constraints of the available micro-CT setup and the necessity to reduce the specimen size to enhance the resolution of the CT images.

Immediately after filling the jars, the samples were subjected to the first micro-CT session. During the micro-CT sessions, the air-tight lids were placed to prevent water evaporation. Subsequently, the specimens were allowed to dry under temperature and humidity conditions similar

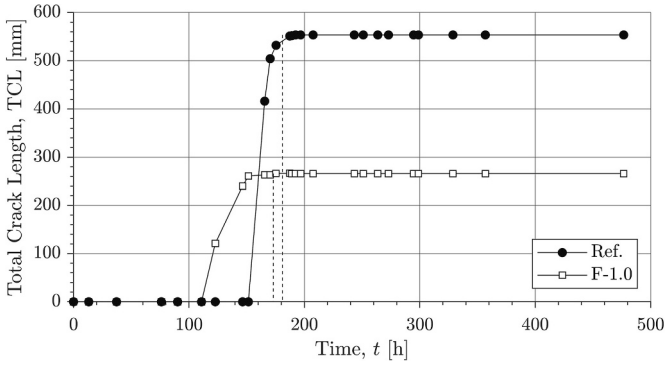

Fig. 9. Total crack length evolution of the reference specimen and the specimen with 1.0% of SAH type F. The dashed lines indicate the fitted time t_1 reported in Table 3.

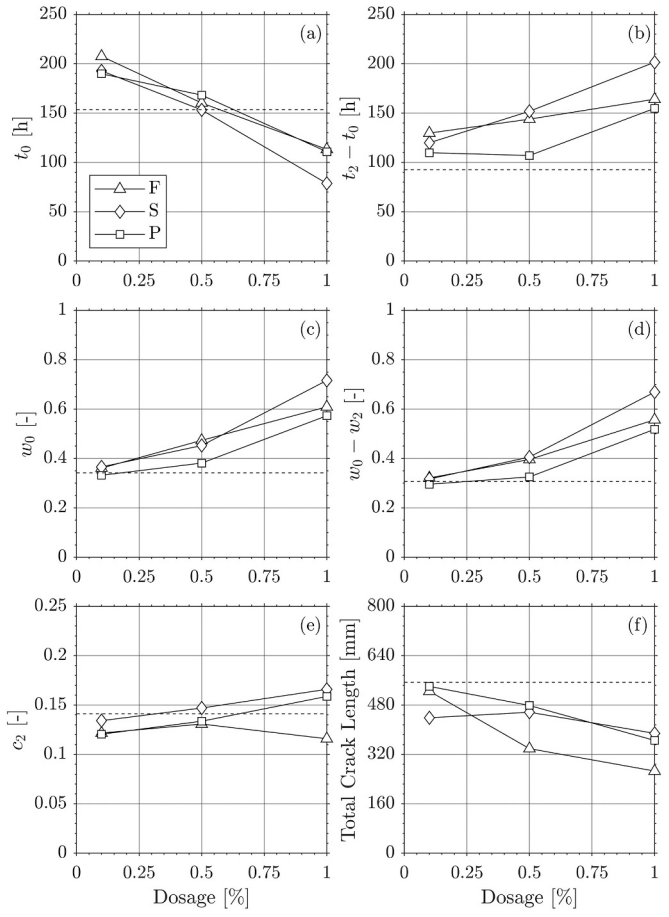

Fig. 10. Cracking evolution parameters as a function of SAH type and dosage. The dashed lines indicate the results for the reference specimen.

to those in the previously discussed desiccation cracking tests (Sec. 3.1). The specimens were weighed regularly to track the evolution of the water content. Three additional micro-CT were performed as the desiccation progressed. Once constant weight was reached for both specimens, water was added to recover the initial water content, placing the airtight lids for two days to ensure rehydration before a new drying process. Two additional micro-CT sessions were carried out: one immediately before removing the lids and the other after significant drying had occurred. The same micro-CT system and settings as previously described (Sec. 3.1) were used in all cases. The reconstruction of the micro-CT volumes and the image treatment were carried out with Avizo software (Thermo Fisher Scientific, 2020). Similar time-lapse CT imaging studies of soil desiccation cracking have been conducted by Tang et al. (2019) and Zaidi et al. (2021).

4.2. Results

Fig. 12 shows 10 × 25 mm vertical slice images obtained via X-ray micro-CT of the two specimens at different times during the drying and wetting cycle.

With reference to the initial state ($w = 60\%$), air bubbles are visible as black circular spherical zones in both reference and treated specimens. In the specimen with SAH, the hydrated SAH particles are clearly distinguished as dark-grey zones with angular shapes. These angular shapes correspond well to those observed for the dry SAH particles (Fig. 1, type F), although the size of the hydrated particles is bigger. Moreover, the dark-grey colour indicates an intermediate density between that of air (~0.001 g/cm^3) and that of the wet soil (~1.65 g/cm^3), which corresponds well to the expected density of the hydrated SAH. Due to the high amount of water absorbed per unit weight and the already close to unity dry density (~1.1 g/cm^3), the density of the hydrated SAH particles should be close to 1 g/cm^3.

In the second scanning session ($w \approx 40\%$), the number of trapped air bubbles in both specimens decreased, particularly in the upper part of the image. Moreover, their shape has become elliptical (ellipsoidal), with the shorter axis aligned with the vertical direction. Similarly, the hydrated SAH particles exhibit a comparable flattening and a slight reduction in size.

With further drying, the dark-grey angular features in the specimen with SAH transition to black, indicating that the space previously occupied by the hydrated SAH is now mainly filled by air. Notably, at this stage, the soil fabric looks very similar to the one shown for the sample treated with 0.5% of SAH type F (Fig. 11). More interestingly, the treated sample does not exhibit the formation of a surficial compacted crust, as observed in the reference soil ($w = 14\%$ and $w = 6\%$), suggesting a more uniform distribution of water content due to a slower evaporation rate (Tollenaar et al., 2018).

The re-wetting to the initial water content leads to generalised cracking in both specimens, as also observed by Tang et al. (2011a). The cracks are predominantly sub-horizontal, although with an increasing vertical component as they approach the container walls. Even after re-wetting, the spherical/ellipsoidal voids remain in both specimens. Notably, there are no angular-shaped voids in the specimen with SAH but rather re-hydrated SAH particles, confirming the association of

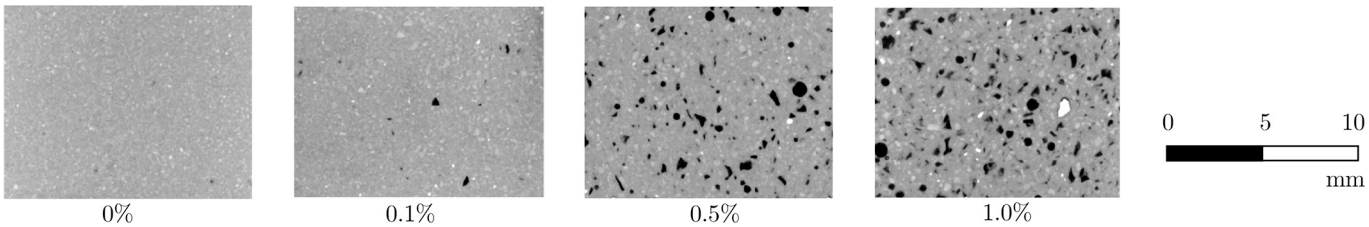

Fig. 11. Micro-CT horizontal cross-section images (10 × 13 mm) of the reference specimen and specimens prepared with SAH type F, at the end of the desiccation cracking test.

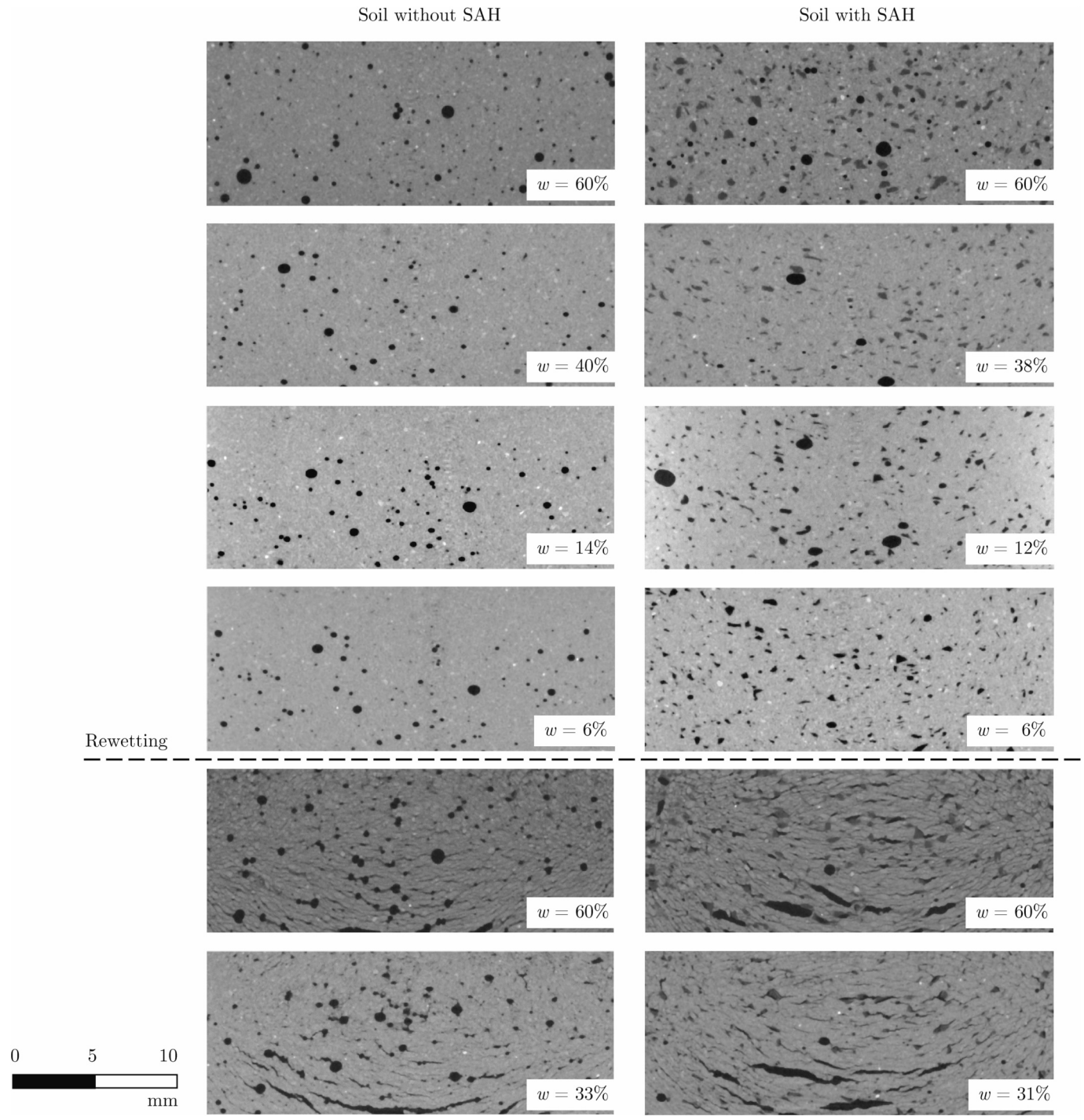

Fig. 12. Vertical micro-CT cross-section images of slurry specimens during drying and re-wetting. Left, reference (plain soil) specimen. Right, specimen with 0.35% addition of SAH type F.

angular voids with SAH particles. The cracking pattern upon re-wetting appears to be affected by the SAH particles. Cracks do not propagate through the SAH particles but along the SAH-soil interfaces. In many cases, this leads to crack branching around the SAH particle, which overlaps the general sub-horizontal cracking. In both specimens for $w \approx 60\%$, water can be distinguished filling the narrower cracks and forming menisci at the tip of the bigger cracks. However, after re-drying to $w \approx 32\%$, the crack filling water disappears in both specimens. In contrast, the presence of re-hydrated SAH particles is still evident in the treated soil.

5. Shrinkage and retention behaviour

5.1. Methods

Desiccation cracking tests have been integrated with the characterisation of the shrinkage and retention behaviour of both untreated and treated soils with SAH. Experimental data from the drying tests using the HYPROP device (METER Group, A, 2018a), Dew Point Potentiometer WP4C (METER Group, A, 2018b) and shrinkage tests were combined to estimate the water retention capacity of the soil fabric over a wide range of suction. In the following, suction measurements from the HYPROP

and the WP4C are combined in the retention curve assuming negligible osmotic suction.

The HYPROP device consists of a main sensor unit comprising two mini-tensiometers with an accuracy of 0.15 kPa. A stainless steel ring (Ø80 × 50 mm) is used to contain the soil sample which is placed on top of the sensor unit (Fig. 13a). The entire setup sits on top of a weighing scale with a precision of 0.1 g. The air-entry value of the ceramic tips is 880 kPa, but due to cavitation of the water in the tensiometer shafts, the maximum suction that can be measured is typically 100 kPa (METER Group, A, 2018a). However, careful saturation of the ceramic tips in demineralised de-aired water can extend the measurement range to around 160 kPa (Tollenaar et al., 2018). Typically, the tensiometer shafts have different lengths to measure water potential at different depths. However, in this study, two short shafts were used to account for the large shrinkage of the sample and to avoid possible exposure of the long shaft to the atmosphere. In addition, the inner side of the steel ring was coated with a thin layer of silicone oil to minimise the adhesion of the sample during the drying process (Fig. 13b).

The Dew Point Potentiometer uses the chilled mirror dew point technique to measure the water potential of the soil by measuring the vapour pressure of the air in equilibrium with the sample in a sealed measurement chamber. The theoretical measurement range spans from 0 to 300 MPa. However, the accuracy of the device below 0.5 MPa is low, which may affect the reliability of the measurements (Ponzoni et al., 2021).

The sample preparation followed the same procedure as the desiccation cracking tests. The tests were conducted on two slurry specimens: reference soil without SAH and treated soil with 0.1% of SAH type F. The choice of this treated soil was based on its superior performance in the desiccation cracking tests, evaluated in terms of reduction of the CIF and reduction of evaporation rate, compared to other SAH types and dosages. Both specimens were prepared and tested with the same procedure. The slurry was prepared with an initial average water content $w = 100\%$ and left in a container overnight to guarantee hydration. After this resting period, any segregated water was removed and the slurry was poured into the HYPROP device all the way to the top of the ring. The HYPROP measurements started immediately and continued as the specimen dried at similar room conditions as for the desiccation cracking tests (Sec. 3.1). Once the HYPROP test was finished, the soil sample was dismounted and a small portion was collected for the WP4C measurements. The remaining material was oven-dried at 105 °C for 24 h to determine the final water content.

In parallel, free shrinkage tests were conducted on replica specimens, two without SAH and other two with 0.1% of SAH type F. For this purpose, the slurries with $w = 100\%$ were poured in Ø50 × 30 mm PTFE (polytetrafluoroethylene) cups coated with silicone oil to minimise adhesion. Subsequently, the specimens were regularly weighed (±0.1 g) and measured (±0.1 mm) as they dried at the same room conditions of the previous tests. During the tests, the specimens shrunk without cracking, preserving their cylindrical shape. Initially, the specimens only experienced shrinkage in the vertical direction, but eventually, the shrinkage became three-dimensional as suction developed. The height changes were determined as the average of five measurements using a depth calliper, while the diameter changes were obtained as the average of four measurements using a regular length calliper.

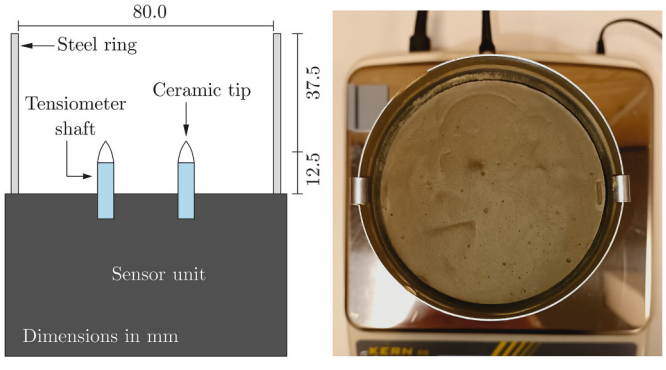

Fig. 13. Schematic diagram of HYPROP showing internal dimensions (a) and (b) impression of the reference soil sample during drying in the HYPROP setup.

5.2. Results

The shrinkage curves obtained from the reference and treated soil are presented in Fig. 14 in terms of average void ratio (e) and water ratio ($e_w = wG_s$). Both void ratio and water ratio are defined with reference to

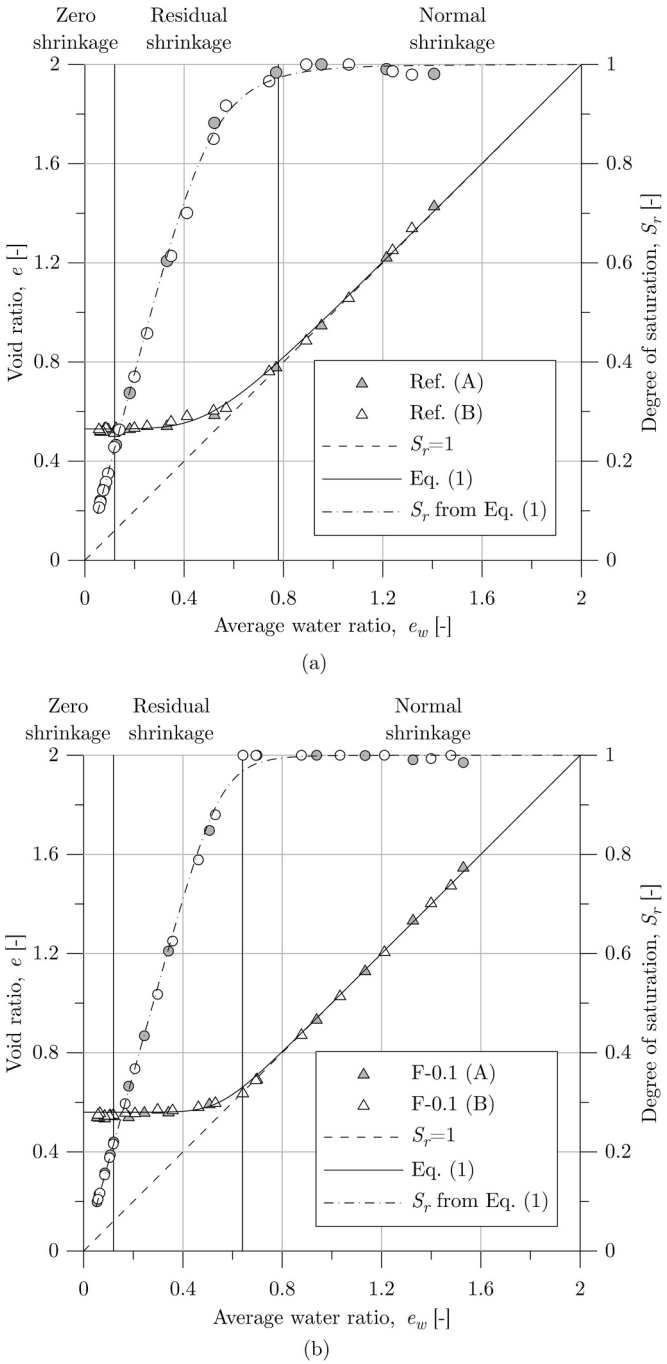

Fig. 14. Shrinkage curves for (a) reference soil and (b) soil with 0.1% SAH type F.

the volume of dry soil particles. Two specimens (A and B) were tested for each type of slurry, showing good repeatability. The data can be interpolated with the expression proposed by Fredlund et al. (2002), which has been rewritten in terms of the average water ratio as follows:

$$e = a\left[\left(\frac{e_w}{a}\right)^c + 1\right]^{\frac{1}{c}} \quad (1)$$

where a represents the minimum void ratio and c controls the curvature of the shrinkage curve. The fitting parameters for Eq. (1) are reported in Table 4. Additionally, Eq. (1) is used to estimate the degree of saturation during the shrinkage test, $S_r = e_w/e$. The comparison with the experimental data is displayed in the secondary vertical axis in Fig. 14.

The shrinkage curve of the reference soil presents three distinct stages (Sun and Cui, 2018): normal shrinkage, where the soil shrinks while remaining almost fully saturated ($e_w > 0.78$); residual shrinkage, accompanied by desaturation ($0.12 < e_w < 0.78$); and zero shrinkage ($e_w < 0.12$). Compared to the reference soil, the treated soil presents a longer normal shrinkage stage ($e_w > 0.64$) and a shorter residual shrinkage stage before reaching the zero shrinkage stage at the same water ratio ($e_w < 0.12$). Additionally, consistent with the desiccation cracking tests, the final void ratio for the treated soil is slightly higher than for the reference soil, 0.56 and 0.53, respectively.

The experimental data from the drying tests were combined with the shrinkage curves in Fig. 14 to obtain the water retention response, linking the degree of saturation (S_r) to the suction (s) over drying. The retention curves are displayed in Fig. 15.

The water retention data are fitted using the modified form of the van Genuchten (1980) expression proposed by Romero and Vaunat (2000):

$$S_r = C(s)\left[\frac{1}{1+(\alpha s)^n}\right]^m; \quad C(s) = 1 - \frac{ln\left(1+\frac{s}{d}\right)}{ln2} \quad (2)$$

In this equation, the parameters m, n and α control the shape of the retention function, as in the original van Genuchten expression. The inverse of parameter α is related to the air-entry value of the soil in a drying path. The additional factor $C(s)$ makes the curve tend to a linear relationship between the logarithm of s and S_r in the high-suction zone, with the parameter d being the suction at $S_r = 0$ (Romero and Jommi, 2008). The fitting parameters for Eq. 2 are reported in Table 4.

The retention data in Fig. 15 reveals that, at high degrees of saturation ($S_r > 0.9$), the soil treated with 0.1% SAH is capable to sustain higher suction than the reference soil, without significant desaturation. By examining Fig. 15, it is possible to estimate the air entry value, conventionally defined as the suction at $S_r = 0.95$, to be approximately 100 kPa for the reference soil and 200 kPa for the treated soil. It can be observed that for suctions exceeding 1.0 MPa, the presence of SAH does not appear to alter the retention behaviour.

6. Discussion

6.1. Role of SAH in the shrinkage and retention response

The experimental data from the shrinkage and HYPROP tests indicate that the presence of SAH alters the initial response of the soil upon drying, particularly in the low suction domain ($s < 150$ kPa). These

Table 4
Fitting parameters of the shrinkage (Eq. (1)) and retention (Eq. (2)) curves.

Parameter	Reference soil	Treated soil (F-0.1)
a	0.53	0.56
c	5.0	8.5
d	2693 MPa	2693 MPa
α	0.50 MPa^{-1}	1.83 MPa^{-1}
m	0.71	0.26
n	0.84	1.70

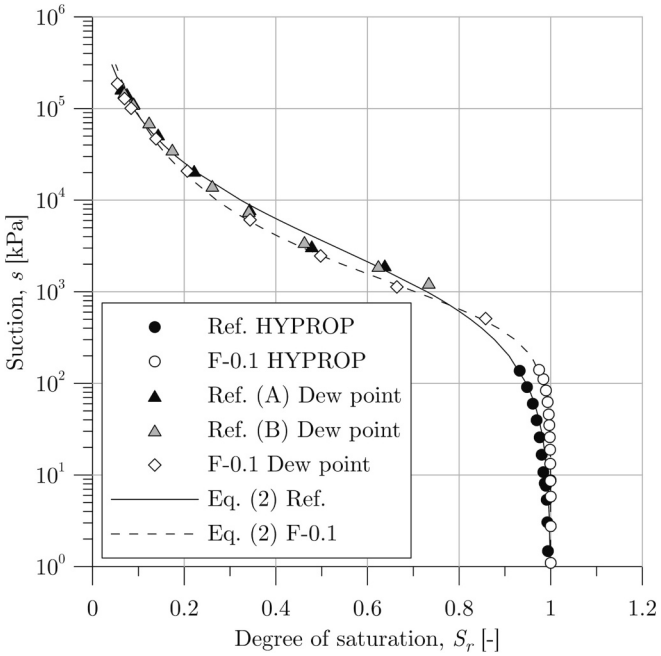

Fig. 15. Soil water retention curve for reference soil and soil with 0.1% SAH type F.

experimental findings, combined with the fabric evidence obtained from the micro-CT scans in Fig. 12, suggest that SAH acts as an internal temporary reservoir capable of supplying the surrounding soil matrix with water. This mechanism is depicted schematically in Fig. 16.

During the first part of the drying process, as the soil dries and shrinks, suction develops in the soil matrix, triggering water uptake from the SAH (Fig. 16b). Consequently, the SAH particles shrink while maintaining the soil matrix saturated for a longer period compared to untreated soil (normal shrinkage stage in Fig. 14b). The rate of suction development measured in the HYPROP tests for both reference and treated soils (Fig. 17), confirms a slower rate of suction built up under the same external conditions, as a result of the water exchange between the soil matrix and the SAH. Worth noticing, the measured suction shows a small drop at about 100 h and 150 h for both untreated and treated soils. Visual inspection of the tests indicates that these drops coincide with the detachment of the samples from the stainless steel ring. As previously observed by Tollenaar (2017), this detachment induces a transient increase in pore pressure and, therefore, a reduction in suction.

During the residual shrinkage stage, as the overall soil volume continues to dry and stiffen, the shrinkage of the soil matrix and of the SAH become incompatible. This results in the formation of partially empty cavities where only a portion of the cavities is occupied by the SAH particles (Fig. 16c). With further drying, the soil eventually approaches the zero shrinkage stage, where water mass loss is not accompanied by further volume reduction (Fig. 16d). Micro-CT scan images obtained during the advanced stages of drying reveal the presence of empty cavities that were previously filled with hydrated SAH, and which are now occupied by air (Fig. 12c).

6.2. Onset of cracking and cracking stages

The results of the desiccation tests reveal four distinct cracking stages common for all the specimens: Stage 0, where drying and shrinkage occur without visible cracking; Stage 1 and Stage 2, where cracks develop and the CIF increases with decreasing water content; and Stage 3, where the CIF levels off (Fig. 7). The transition between these different stages is modified by the addition of SAH. On one hand, the

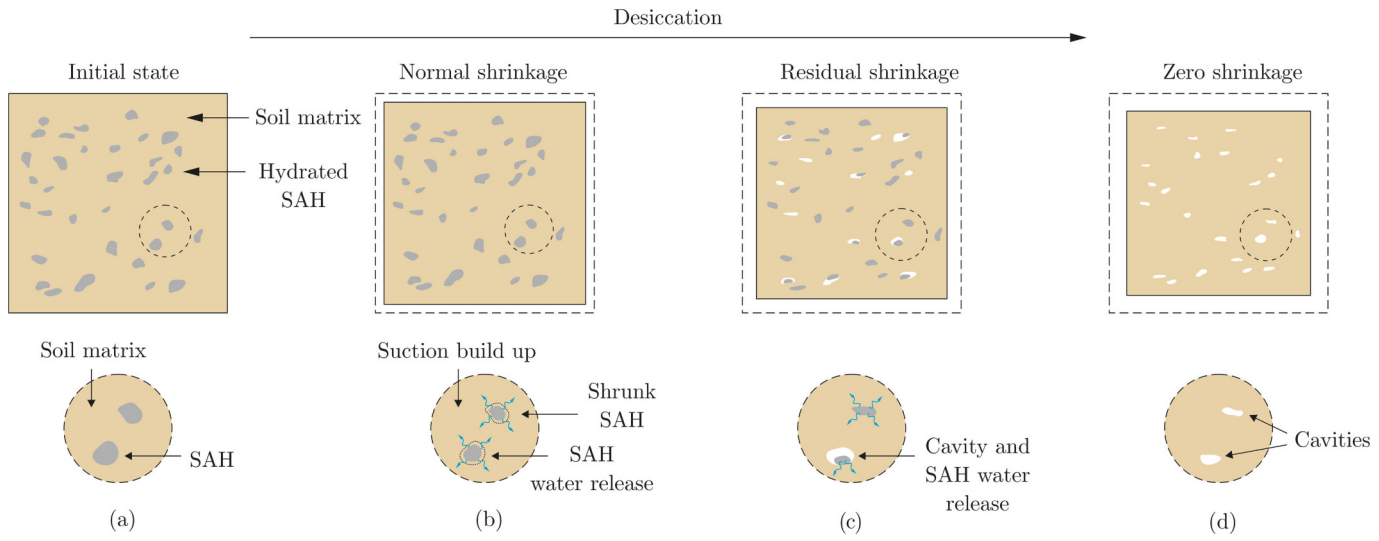

Fig. 16. Schematics of the interaction between the soil matrix and the SAH particles during desiccation.

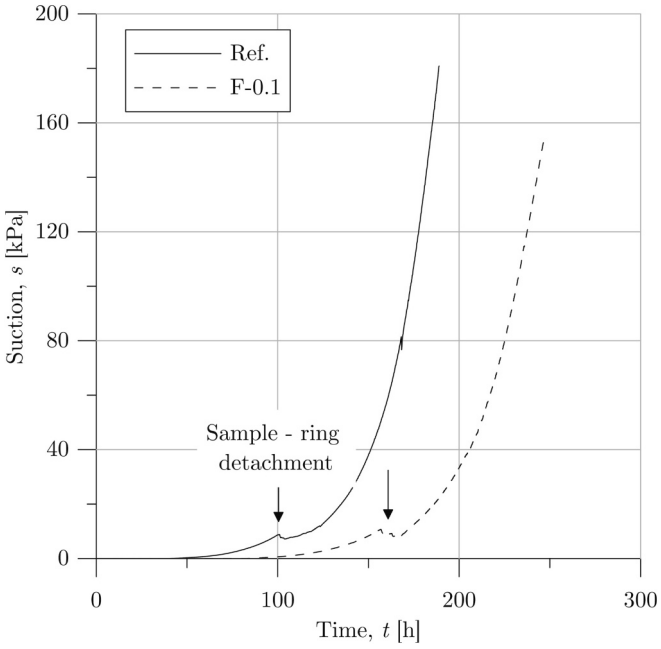

Fig. 17. Time evolution of the measured suction in the HYPROP for reference and treated soil with 0.1% SAH type F.

average water content at cracking initiation increases with the dosage of SAH (Fig. 10c). On the other hand, the addition of SAH expands the range of water content over which crack development occurs (Fig. 10d). In comparison to untreated soil, the final CIF consistently decreases for the lowest SAH dosage of 0.1%, albeit to varying extents depending on the type of SAH used (Fig. 10e). However, with higher dosage of SAH, 0.5% and 1.0% the CIF tends to increase. This observed effect could be linked to a significant change in the soil matrix due to the abundance of large cavities initially occupied by SAH, as observed in Fig. 11 for the 0.5% and 1.0% dosages. These cavities could lead to crack initiation and branching, as previously observed by Costa et al. (2013); Shin and Santamarina (2011); Tang et al. (2021). In comparison to untreated soil, the application of increasing dosages of SAH results in a decrease in the TCL, with fewer but wider cracks. At the current stage of this research, the origins of the quantitative difference observed in the CIF and TCL are not yet fully understood. Possible reasons may come from the characteristics of the SAH types. More research in this direction should be done to confirm these observations.

Further insight into the cracking process is provided by combining the experimental observations from desiccation cracking tests with shrinkage and retention data. This combined analysis is performed under the assumption that the shrinkage and retention curves presented in Sec. 5 are representative of the response of the bulk soil in the desiccation cracking tests. The fact that no cracks were observed in the shrinkage and retention tests permits this assumption.

Fig. 18a displays the evolution of the CIF along with the average water ratio for the untreated reference specimen and the specimen treated with 0.1% SAH type F. The average water ratio at the onset of visible cracking is $e_w = 0.89$ and $e_w = 0.95$, respectively. Projection of these water ratios onto the corresponding retention curves (Fig. 18b) and shrinkage curves (Fig. 15), locates the onset of cracking within the normal shrinkage stage (reference specimen: $s \approx 10$ kPa, $S_r = 0.99$; treated specimen: $s \approx 16$ kPa, $S_r \approx 1.0$). These results are in agreement with previous studies that have identified the onset of cracking when the soil is still substantially saturated, with $S_r > 0.98$ (Shin and Santamarina, 2011; Tang et al., 2011a, 2011b).

At the beginning of cracking (Stage 1 in Fig. 18a), the CIF increases rapidly as the average water ratio and pore volume decrease. It is worth noting that the inclusion of SAH appears to mitigate the rate at which the CIF rises with water loss. At the end of Stage 1, the CIF values are approximately 0.106 and 0.086, while the final values at the end of drying are 0.141 and 0.122, for the reference and treated soils, respectively. These findings indicate that approximately 75% and 70% of the total cracked area is formed during Stage 1, which is characterised by a suction level below 150 kPa and a state close to saturation ($S_r > 0.93$ for the reference soil, $S_r > 0.97$ for the treated soil).

Beneficial effects of decreasing the evaporation rate on the cracking process have been reported by Tang et al. (2010) and Uday and Singh (2013), with desiccation cracking tests conducted at different temperatures and relative humidity, respectively. In the case of the results presented in Fig. 18, the lower CIF observed for the treated soil can be associated with a lower evaporation rate (Fig. 5), lower rate of suction build-up (Fig. 17) and higher saturation level (Fig. 15) assured by the inclusion of SAH. The increase in air entry value observed for the treated soil could also anticipate potential impacts on tensile strength (Tollenaar et al., 2017) resulting from the inclusion of SAH although no experimental evidence (e.g., direct tension tests) is available at the moment.

With further drying, the CIF increment rate decreases (Stage 2). The transition between Stage 1 and Stage 2 occurs at average water ratios of $e_w = 0.61$ for the reference soil and $e_w = 0.63$ for the treated soil, cor-

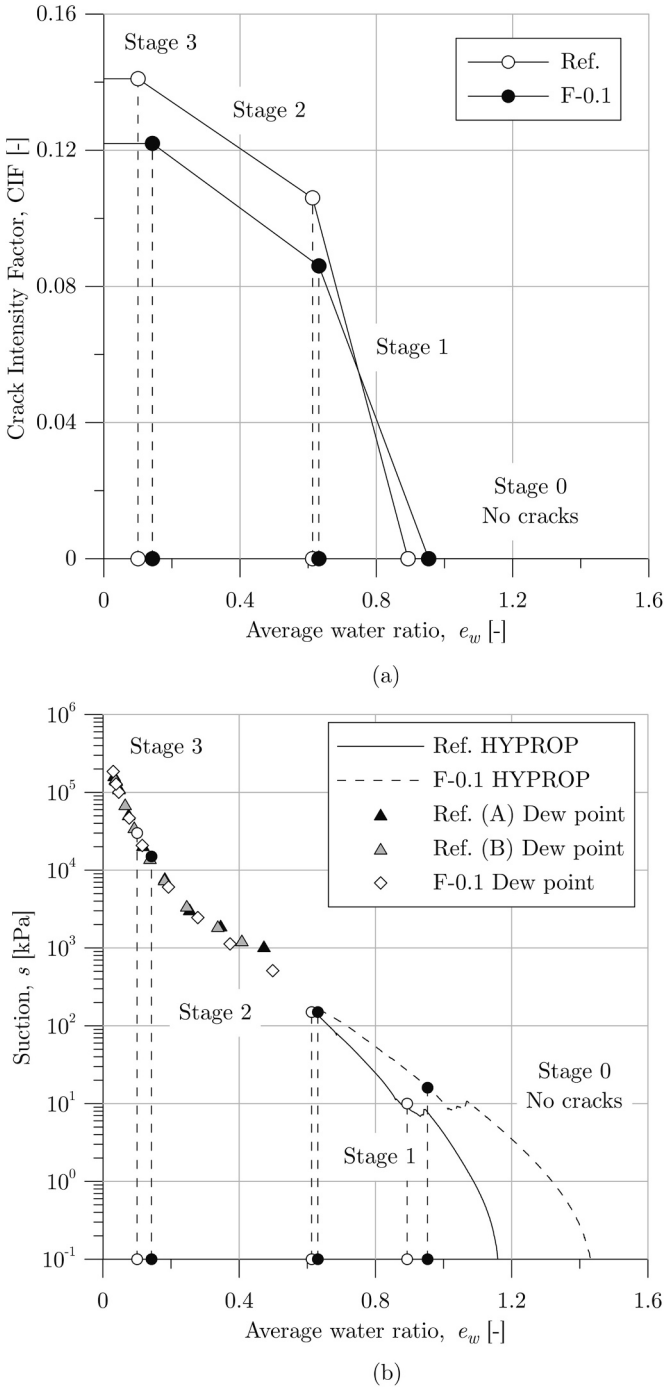

Fig. 18. (a) Crack intensity Factor as a function of the average water ratio for reference and treated soil (F-0.1), and delimitation of the four cracking stages; (b) projection of the cracking stages on the retention curves.

responding to a suction of about 150 kPa. This suction is within the range of the air entry value observed in the retention curves (Fig. 15). The decrease of the CIF rate with decreasing water content after the air entry value has also been observed by Tang et al. (2011b).

As previously introduced, image analysis has revealed that the CIF increment in Stage 2 is not due to the formation of new cracks or propagation of existing ones as in Stage 1, but it is mainly due to the widening of existing cracks (Fig. 9). This phenomenon is further illustrated in Fig. 19, which shows the evolution of the cracking pattern in different stages for both the reference soil and soil treated with 0.1% of type F SAH. Similar observations were reported by Tang et al. (2011c).

In Stage 2, the CIF increases at the same rate for both the treated and untreated soils (Fig. 18b). These results confirm that the effect of the SAH on the soil response is primarily observed in the first drying stages (Stage 0 and Stage 1), for suctions below the air entry value and where the cracking onset and propagation take place.

With further drying, the CIF eventually levels off, configuring Stage 3. This occurs at water ratios of $e_w = 0.1$ for the reference soil and $e_w = 0.14$ for the treated soil. These water ratios are very close to the onset of the zero shrinkage stage ($e_w = 0.12$ in Fig. 14), as previously observed by Tang et al. (2010) and Tang et al. (2011a). In Fig. 18b, Stage 3 is located in the high suction domain of the retention curves ($s > 20$ MPa), where the retention curves for the reference and treated soils coincide.

Additional insights into Stage 3 are offered in Fig. 20, by comparing the retention data in Fig. 18b with the retention data of a natural sample of soil studied. As shown in Fig. 20, for $e_w < 0.2$, all the samples exhibit a similar retention curve, suggesting that the influence of the void ratio on the retention response is negligible. These results locate Stage 3 within the region dominated by adsorptive storage mechanisms, where water is held inside the intra-aggregate porosity (Romero et al., 2011; Romero et al., 1999).

7. Conclusions

Laboratory tests were performed on initially saturated silty soil treated with superabsorbent hydrogels (SAH) to investigate their impact on the retention behaviour and desiccation cracking response. Desiccation cracking tests, shrinkage tests and water retention tests were combined in the attempt to describe the cracking process upon drying and to evaluate the effect of different dosages and types of SAH on the overall soil response. The laboratory tests were complemented with micro-CT scan analyses to offer insights into the soil fabric changes due to the SAH addition. Based on the experimental results, the following conclusions can be drawn:

- The admixed SAH acts as an internal water reservoir, providing a source of water to the soil matrix during the drying process. Compared to the untreated soil, the addition of SAH extends the normal shrinkage stage, during which the soil shrinks while remaining fully saturated. Retention data also indicates that, for degrees of saturation $S_r > 0.9$, the treated soil can maintain a higher level of suction ($s \approx 200$ kPa) compared to the reference soil, without undergoing significant desaturation.
- Compared to the untreated soil, the addition of SAH reduces the evaporation rate. Noteworthy, within the tested dosages, the decrease in the evaporation rate does not exhibit a proportional relationship with the amount of SAH used. The most substantial reduction in the evaporation rate was observed when employing a dosage of 0.1% SAH. Fabric changes caused by the presence of SAH cavities, particularly at high dosages, could create preferential sites for stress concentration and crack initiation.
- The progression of the cracking process was analysed in terms the Crack Intensity Factor (CIF). In both untreated and treated soil, desiccation cracking began when the soil was still considerably saturated, occurring at suctions well before reaching the air entry value. Once cracking initiated, approximately 70% of the cracked area developed during the early stage of drying, within the normal shrinkage stage, and at suctions below 150 kPa. The inclusion of SAH appears to mitigate the rate at which the CIF rises with water loss.
- For suctions exceeding the air entry value, the rate of CIF increment exhibited a similar decrease in both treated and untreated soils. Image analyses confirmed that the increase in CIF during this stage did not result from the formation of new cracks or the propagation of existing ones. Instead, it was primarily attributed to the widening of previous cracks.

Although preliminary, the experimental results presented in this

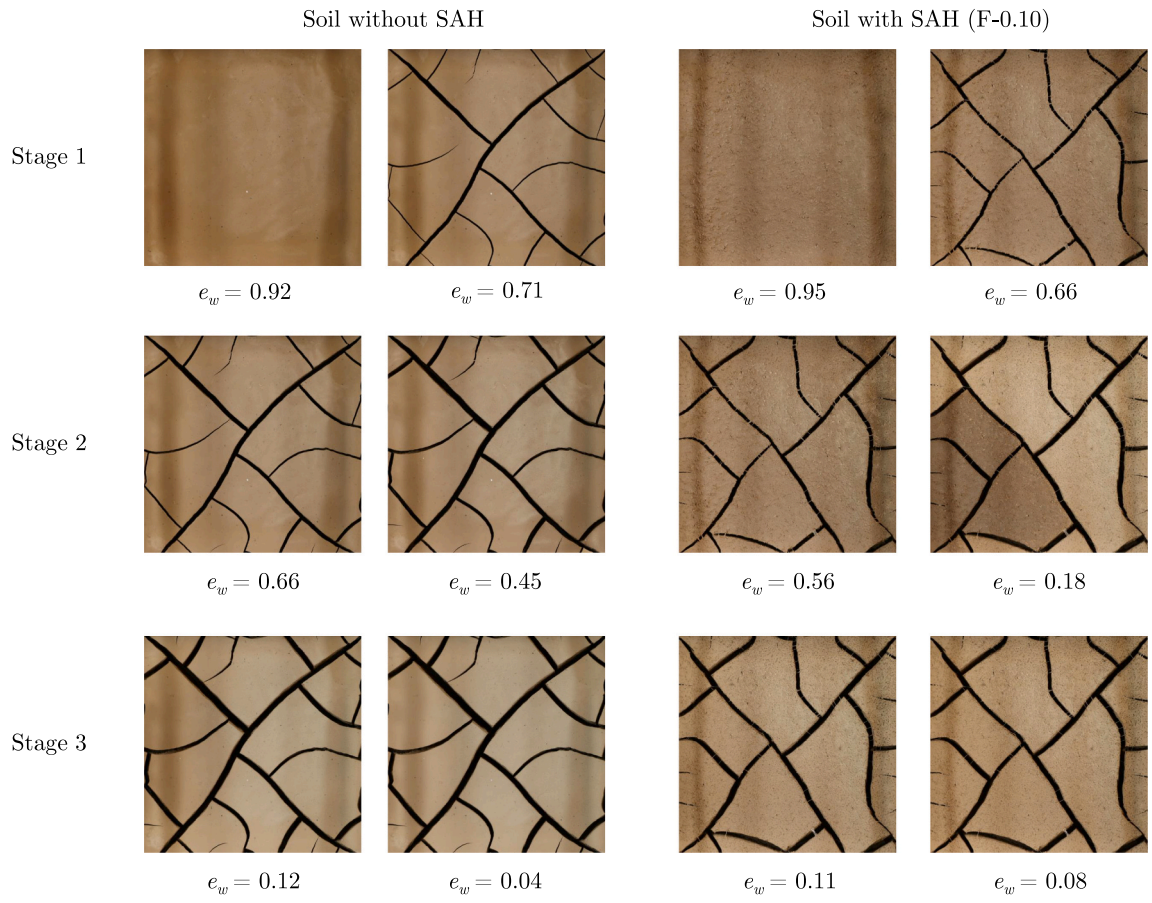

Fig. 19. Evolution of crack patterns for the reference soil and treated soil (F-0.1).

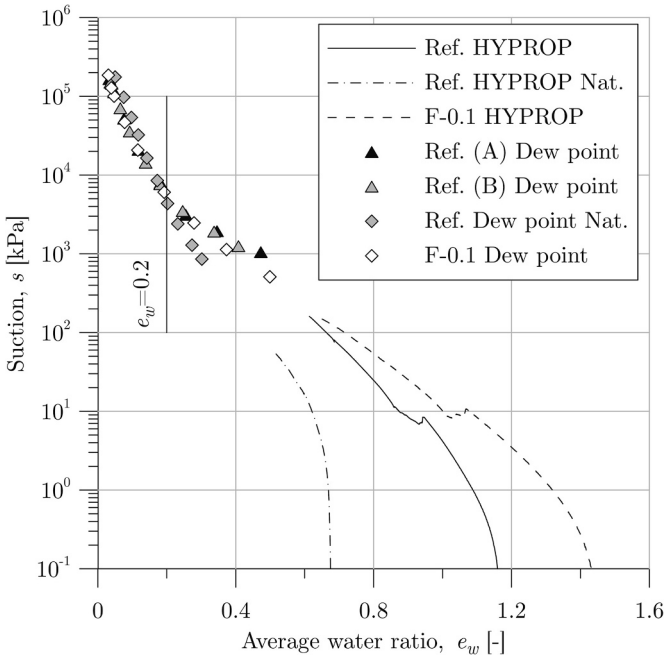

Fig. 20. Comparison of retention curve for natural and reconstituted samples of reference untreated soil.

work suggest the potential of utilising SAH as treatment to enhance soil response upon drought. However, this study indicates that the decreases in evaporation rate and final crack intensity factor are not directly proportional to the dosage of SAH. This observation necessitates further investigation into the impact of SAH inclusion on the soil structure.

Furthermore, additional experimental research is required to assess the effects of SAH on aspects of the soil behaviour not addressed in this study, such as hydraulic conductivity, compressibility and shear strength. Examining these aspects will provide a more comprehensive understanding of the effects of SAH on soil behaviour and its potential as a soil treatment method.

CRediT authorship contribution statement

Joaquín Liaudat: Writing – review & editing, Writing – original draft, Visualization, Validation, Software, Methodology, Investigation, Formal analysis, Data curation, Conceptualization. **Stefano Muraro:** Writing – review & editing, Writing – original draft, Visualization, Validation, Supervision, Project administration, Methodology, Investigation, Funding acquisition, Formal analysis, Data curation, Conceptualization.

Declaration of competing interest

The authors declare that they have no known competing financial interests or personal relationships that could have appeared to influence the work reported in this paper.

Data availability

Data will be made available on request.

Acknowledgements

The financial support of the Dutch Organisation for Scientific Research (NWO), under the project "Bio-inspired 'bubble gum' to prevent cracks in soils" with project number OCENW.XS4.238 is gratefully acknowledged. The first author has received funding from the European Union's Horizon 2020 research and innovation programme under the Marie Skłodowska-Curie grant agreement No. 101028292. The authors thank the fruitful discussions with Prof. Cristina Jommi during the development of this research.

References

Andry, H., Yamamoto, T., Irie, T., Moritani, S., Inoue, M., Fujiyama, H., 2009. Water retention, hydraulic conductivity of hydrophilic polymers in sandy soil as affected by temperature and water quality. J. Hydrol. 373, 177–183. https://doi.org/10.1016/j.jhydrol.2009.04.020.

ASTM, 2014. ASTM D5550-14 Standard test method for specific gravity of soil solids by gas pycnometer. In: Annual Book of ASTM Standards. American Society of Testing and Materials.

Bakass, M., Mokhlisse, A., Lallemant, M., 2002. Absorption and desorption of liquid water by a superabsorbent polymer: effect of polymer in the drying of the soil and the quality of certain plants. J. Appl. Polym. Sci. 83, 234–243. https://doi.org/10.1002/app.2239.

Banedjschafie, S., Durner, W., 2015. Water retention properties of a sandy soil with superabsorbent polymers as affected by aging and water quality. J. Plant Nutr. Soil Sci. 178, 798–806. https://doi.org/10.1002/jpln.201500128.

Bao, Y., Ma, J., Li, N., 2011. Synthesis and swelling behaviors of sodium carboxymethyl cellulose-g-poly(AA-co-AM-co-AMPS)/MMT superabsorbent hydrogel. Carbohydr. Polym. 84, 76–82. https://doi.org/10.1016/j.carbpol.2010.10.061.

BS, 1996. BS1377:1996 Methods of Test for Soils for Civil Engineering Purposes Part 2. Classification Tests. British Standard Institution, London.

Chan, T.F., Vese, L.A., 2001. Active contours without edges. IEEE Trans. Image Process. 10, 266–277. https://doi.org/10.1109/83.902291.

Cheng, W.M., Hu, X.M., Zhao, Y.Y., Wu, M.Y., Hu, Z.X., Yu, X.T., 2017. Preparation and swelling properties of poly(acrylic acid-co-acrylamide) composite hydrogels. E-Polymers 17, 95–106. https://doi.org/10.1515/epoly-2016-0250.

Cheng, Q., Tang, C.S., Guo Chen, Z., El-Maarry, M.R., Zeng, H., Shi, B., 2020. Tensile behavior of clayey soils during desiccation cracking process. Eng. Geol. 279, 105909 https://doi.org/10.1016/j.enggeo.2020.105909.

Corte, A.E., Higashi, A., 1964. Experimental research on desiccation cracks in soils. In: CRREL Research Report, 72. URL. http://trid.trb.org/view.aspx?id=136592.

Costa, S., Kodikara, J., Shannon, B., 2013. Salient factors controlling desiccation cracking of clay in laboratory experiments. Geotechnique 63, 18–29. https://doi.org/10.1680/geot.9.P.105.

Dorraji, S.S., Golchin, A., Ahmadi, S., 2010. The effects of hydrophilic polymer and soil salinity on corn growth in sandy and loamy soils. Clean (Weinh) 38, 584–591. https://doi.org/10.1002/clen.201000017.

Feng, D., Bai, B., Ding, C., Wang, H., Suo, Y., 2014. Synthesis and swelling behaviors of yeast-g-poly(acrylic acid) superabsorbent co-polymer. Ind. Eng. Chem. Res. 53, 12760–12769. https://doi.org/10.1021/ie502248n.

Fredlund, M.D., Wilson, G.W., Fredlund, D.G., 2002. Representation and estimation of the shrinkage curve. In: 3rd International Conference on Unsaturated Soils, UNSAT 2002, pp. 145–149.

Ismail, H., Irani, M., Ahmad, Z., 2013. Starch-based hydrogels: present status and applications. Int. J. Polym. Mater. Polym. Biomater. 62, 411–420. https://doi.org/10.1080/00914037.2012.719141.

Khan, M.S., Hossain, S., Ahmed, A., Faysal, M., 2017. Investigation of a shallow slope failure on expansive clay in Texas. Engineering Geology 219, 118–129. https://doi.org/10.1016/j.enggeo.2016.10.004.

Koupai, J.A., Eslamian, S.S., Kazemi, J.A., 2008. Enhancing the available water content in unsaturated soil zone using hydrogel, to improve plant growth indices. Ecohydrol. Hydrobiol. 8, 67–75. https://doi.org/10.2478/v10104-009-0005-0.

Li, J.H., Lu, Z., Guo, L.B., Zhang, L.M., 2017. Experimental study on soil-water characteristic curve for silty clay with desiccation cracks. Engineering Geology 218, 70–76. https://doi.org/10.1016/j.enggeo.2017.01.004.

Liao, R., Wu, W., Ren, S., Yang, P., 2016. Effects of Superabsorbent Polymers on the Hydraulic Parameters and Water Retention Properties of Soil. J. Nanomater. 2016 https://doi.org/10.1155/2016/5403976.

Louf, J.F., Lu, N.B., O'Connell, M.G., Cho, H.J., Datta, S.S., 2021. Under pressure: Hydrogel swelling in a granular medium. Science Advances 7, 1–11. https://doi.org/10.1126/sciadv.abd2711.

METER Group, A, 2018a. HYPROP User Manual V 2018/3. Munich, Germany.

METER Group, A, 2018b. WP4C Dew Point PotentiaMeter operator's Manual 2018. Munich, Germany.

Montesano, F.F., Parente, A., Santamaria, P., Sannino, A., Serio, F., 2015. Biodegradable Superabsorbent Hydrogel increases Water Retention Properties of growing Media and Plant Growth. Agriculture and Agricultural Science Procedia 4, 451–458. https://doi.org/10.1016/j.aaspro.2015.03.052.

Morris, P.H., Graham, J., Williams, D.J., 1992. Cracking in drying soils. Canadian Geotechnical Journal 29, 263–277. https://doi.org/10.1139/t92-030.

Narjary, B., Aggarwal, P., Singh, A., Chakraborty, D., Singh, R., 2012. Water availability in different soils in relation to hydrogel application. Geoderma 187-188, 94–101. https://doi.org/10.1016/j.geoderma.2012.03.002.

Peron, H., Hueckel, T., Laloui, L., Hu, L.B., 2009. Fundamentals of desiccation cracking of fine-grained soils: Experimental characterisation and mechanisms identification. Can. Geotech. J. 46, 1177–1201. https://doi.org/10.1139/T09-054.

Ponzoni, E., Nocilla, A., Jommi, C., 2021. Determination of water retention properties of silty sands by means of combined commercial techniques. Geosciences (Switzerland) 11, 1–11. https://doi.org/10.3390/geosciences11080315.

Qi, C., Bai, Y., Liu, J., Bu, F., Kanungo, D.P., Song, Z., He, X., 2020. Desiccation cracking behavior of polyurethane and polyacrylamide admixed clayey soils. Polymers 12, 1–18. https://doi.org/10.3390/polym12102398.

Rizwan, M., Rubina Gilani, S., Iqbal Durani, A., Naseem, S., 2021. Materials diversity of hydrogel: Synthesis, polymerization process and soil conditioning properties in agricultural field. J. Adv. Res. 33, 15–40. https://doi.org/10.1016/j.jare.2021.03.007.

Romero, E., Jommi, C., 2008. An insight into the role of hydraulic history on the volume changes of anisotropic clayey soils. Water Resour. Res. 44, 1–16. https://doi.org/10.1029/2007WR006558.

Romero, E., Vaunat, J., 2000. Retention curves of deformable clays. In: Experimental evidence and Theoretical Approaches in Unsaturated Soils. Balkema, Rotterdam, pp. 91–106.

Romero, E., Gens, A., Lloret, A., 1999. Water permeability, water retention and microstructure of unsaturated compacted Boom clay. Engineering Geology 54, 117–127. https://doi.org/10.1016/S0013-7952(99)00067-8.

Romero, E., Della Vecchia, G., Jommi, C., 2011. An insight into the water retention properties of compacted clayey soils. Geotechnique 61, 313–328. https://doi.org/10.1680/geot.2011.61.4.313.

Saha, A., Rattan, B., Sekharan, S., Manna, U., 2020a. Quantifying the interactive effect of water absorbing polymer (WAP)-soil texture on plant available water content and irrigation frequency. Geoderma 368, 114310. https://doi.org/10.1016/j.geoderma.2020.114310.

Saha, A., Sekharan, S., Manna, U., 2020b. Superabsorbent hydrogel (SAH) as a soil amendment for drought management: A review. Soil Tillage Res. 204, 104736 https://doi.org/10.1016/j.still.2020.104736.

Shin, H., Santamarina, J.C., 2011. Desiccation cracks in saturated fine-grained soils: Particle-level phenomena and effective-stress analysis. Geotechnique 61, 961–972. https://doi.org/10.1680/geot.8.P.012.

Song, W.K., Cui, Y.J., 2020. Modelling of water evaporation from cracked clayey soil. Engineering Geology 266, 105465. https://doi.org/10.1016/j.enggeo.2019.105465.

Spagnol, C., Rodrigues, F.H., Neto, A.G., Pereira, A.G., Fajardo, A.R., Radovanovic, E., Rubira, A.F., Muniz, E.C., 2012. Nanocomposites based on poly(acrylamide-co-acrylate) and cellulose nanowhiskers. Eur. Polym. J. 48, 454–463. https://doi.org/10.1016/j.eurpolymj.2011.12.005.

Sun, W.J., Cui, Y.J., 2018. Investigating the microstructure changes for silty soil during drying. Geotechnique 68, 370–373. https://doi.org/10.1680/jgeot.16.P.165.

Taheri, S., El-zein, A., 2023. Desiccation cracking of polymer-bentonite mixtures: an experimental investigation. Applied Clay Science 238, 106945. https://doi.org/10.1016/j.clay.2023.106945.

Tang, C.S., Cui, Y.J., Tang, A.M., Shi, B., 2010. Experiment evidence on the temperature dependence of desiccation cracking behavior of clayey soils. Engineering Geology 114, 261–266. https://doi.org/10.1016/j.enggeo.2010.05.003.

Tang, C.S., Cui, Y.J., Shi, B., Tang, A.M., Liu, C., 2011a. Desiccation and cracking behaviour of clay layer from slurry state under wetting-drying cycles. Geoderma 166, 111–118. https://doi.org/10.1016/j.geoderma.2011.07.018.

Tang, C.S., Shi, B., Liu, C., Gao, L., Inyang, H.I., 2011b. Experimental Investigation of the Desiccation cracking Behavior of Soil Layers during Drying. J. Mater. Civ. Eng. 23, 873–878. https://doi.org/10.1061/(asce)mt.1943-5533.0000242.

Tang, C.S., Shi, B., Liu, C., Suo, W.B., Gao, L., 2011c. Experimental characterization of shrinkage and desiccation cracking in thin clay layer. Applied Clay Science 52, 69–77. https://doi.org/10.1016/j.clay.2011.01.032.

Tang, C.S., Zhu, C., Leng, T., Shi, B., Cheng, Q., Zeng, H., 2019. Three-dimensional characterization of desiccation cracking behavior of compacted clayey soil using X-ray computed tomography. Engineering Geology 255, 1–10. https://doi.org/10.1016/j.enggeo.2019.04.014.

Tang, C.S., Zhu, C., Cheng, Q., Zeng, H., Xu, J.J., Tian, B.G., Shi, B., 2021. Desiccation cracking of soils: A review of investigation approaches, underlying mechanisms, and influencing factors. Earth Sci. Rev. 216, 103586 https://doi.org/10.1016/j.earscirev.2021.103586.

The MathWorks, 2020. MATLAB Version 9.8.0.1359463 (R2020a). The MathWorks Inc., Natick, MA, USA. URL: https://www.mathworks.com.

Thermo Fisher Scientific, 2020. Avizo (version 2020.3). URL. https://www.thermofisher.com/nl/en/home/electron-microscopy/products/software-em-3d-vis/3d-visualization-analysis-software.html.

Tollenaar, R.N., 2017. Experimental Investigation on the Desiccation and Fracturing of Clay. Doctoral thesis.. Delft University of Technology. https://doi.org/10.4233/uuid:40f6b033-0e6a-460b-9501-30cf35a99b8d.

Tollenaar, R.N., van Paassen, L.A., Jommi, C., 2017. Experimental evaluation of the effects of pull rate on the tensile behavior of a clay. Appl. Clay Sci. 144, 131–140. https://doi.org/10.1016/j.clay.2017.04.026. https://doi.org/10.1016/j.clay.2017.04.026.

Tollenaar, R.N., van Paassen, L.A., Jommi, C., 2018. Small-scale evaporation tests on clay: influence of drying rate on clayey soil layer. Canadian Geotechnical Journal 55, 437–445. https://doi.org/10.1139/cgj-2017-0061.

Uday, K.V., Singh, D.N., 2013. Investigation on cracking Characteristics of Fine-Grained Soils under Varied Environmental Conditions. Drying Technol. 31, 1255–1266. https://doi.org/10.1080/07373937.2013.785433.

van Genuchten, M.T., 1980. A closed-form equation for predicting the hydraulic conductivity of unsaturated soils. Soil Sci. Soc. Am. J. 44, 892–898.

Yu, J., Shi, J.G., Ma, X., Dang, P.F., Yan, Y.L., Mamedov, A.I., Shainberg, I., Levy, G.J., 2017. Superabsorbent Polymer Properties and Concentration Effects on Water Retention under Drying Conditions. Soil Sci. Soc. Am. J. 81, 889–901. https://doi.org/10.2136/sssaj2016.07.0231.

Zaidi, M., Ahfir, N.D., Alem, A., Taibi, S., El Mansouri, B., Zhang, Y., Wang, H., 2021. Use of X-ray computed tomography for studying the desiccation cracking and self-healing of fine soil during drying–wetting paths. Engineering Geology 292, 106255. https://doi.org/10.1016/j.enggeo.2021.106255.

Zhang, J.M., Luo, Y., Zhou, Z., Chong, L., Victor, C., Zhang, Y.F., 2021. Effects of preferential flow induced by desiccation cracks on slope stability. Engineering Geology 288, 106164. https://doi.org/10.1016/j.enggeo.2021.106164.